ACS APPLIED MATERIALS & INTERFACES

www.acsami.org

Research Article

Unraveling the Mechanism of the 150-Fold Photocurrent Enhancement in Plasma-Treated 2D TMDs

Karolina Czerniak-Łosiewicz,* Michał Świniarski, Arkadiusz P. Gertych, Małgorzata Giza, Zofia Maj, Maciej Rogala, Paweł J. Kowalczyk, and Mariusz Zdrojek

Cite This: *ACS Appl. Mater. Interfaces* 2022, 14, 33984−33992

Read Online

ACCESS | Metrics & More | Article Recommendations | Supporting Information

ABSTRACT: Two-dimensional (2D) transition metal dichalcogenides (TMDs) are increasingly investigated for applications such as optoelectronic memories, artificial neurons, sensors, and others that require storing photogenerated signals for an extended period. In this work, we report an environment- and gate voltage-dependent photocurrent modulation method of TMD monolayer-based devices (WS_2 and MoS_2). To achieve this, we introduce structural defects using mild argon−oxygen plasma treatment. The treatment leads to an extraordinary over 150-fold enhancement of the photocurrent in vacuum along with an increase in the relaxation time. A significant environmental and electrostatic dependence of the photocurrent signal is observed. We claim that the effect is a combined result of atomic vacancy introduction and oxide formation, strengthened by optimal wavelength choice for the modified surface. We believe that this work contributes to paving the way for tunable 2D TMD optoelectronic applications.

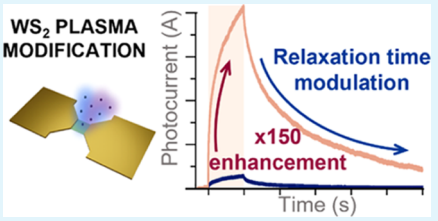

KEYWORDS: *two-dimensional materials, tungsten disulfide, transition metal dichalcogenides, plasma treatment, photocurrent enhancement, surface modification, optoelectronic memories*

INTRODUCTION

Transition metal dichalcogenide (TMD) monolayers have been extensively studied due to a direct band gap responsible for their favorable properties such as a high on/off ratio and efficient electron−hole generation.[1] The optoelectronic properties of TMDs, especially molybdenum disulfide, are of particular interest because of the possibility of creating transparent and elastic photodetectors for wearable electronics.[2] However, owing to the effects such as photogating and persistent photoconductivity, response times vary largely between reports, and often these materials show relatively slow response times.[3−5] These properties could find use in some areas of optoelectronic applications, particularly those where the fast response is not vital.

In recent years, a new, interesting branch called neuromorphic engineering has gained a lot of attention, which aims to emulate the function of biological neurons to do computations.[6] Neuromorphic sensors,[7] optoelectronic synapses,[8] and optoelectronic memories[7,9,10] have been studied on 2D materials to perform computations such as image and pattern recognition, object detection, and storing sensitive information with light, which are all realized by maintaining an electrical signal for a specific time after illumination. In these applications, photogenerated carriers need to be trapped in the active material until they are processed as an electric signal for computational purposes. The mechanism of charge trapping after illumination is terminated, and maintaining the electrical signal is called persistent photoconductivity (PPC), seen previously in TMDs.[3] However, different samples of TMDs show different times of maintaining PPC, from tens of seconds up to even ∼30 days.[11]

Several studies have shown TMDs undergoing plasma treatment to modify their properties. It has been reported that MoS_2 photocurrent can be enhanced by oxygen plasma treatment, and the enhancement was a result of charge trapping at the heterojunction between molybdenum oxide (MoO_3) and MoS_2; however, it occurred only after a single plasma process, and the repetition of the treatment resulted in degradation of the photoresponse.[12] WS_2 samples were also previously subjected to plasma-induced defect formation. There have been reports of photoluminescence enhancement and patching up sulfur vacancies of WS_2 by nitrogen plasma.[13,14] The reduction of WS_2 monolayer-based field-effect transistors' (FETs) threshold voltage and mobility improvement were also seen after treatment with argon plasma due to the creation of sulfur vacancies in the WS_2 layer and removing surface contaminants from the sample.[15] Although some recent works on photocurrent in TMDs highlight the difference between measurements in different environments,[16,17] none of the aforementioned plasma treatment experiments discussed the direct influence of plasma on

Received: April 14, 2022
Accepted: July 8, 2022
Published: July 18, 2022

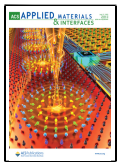

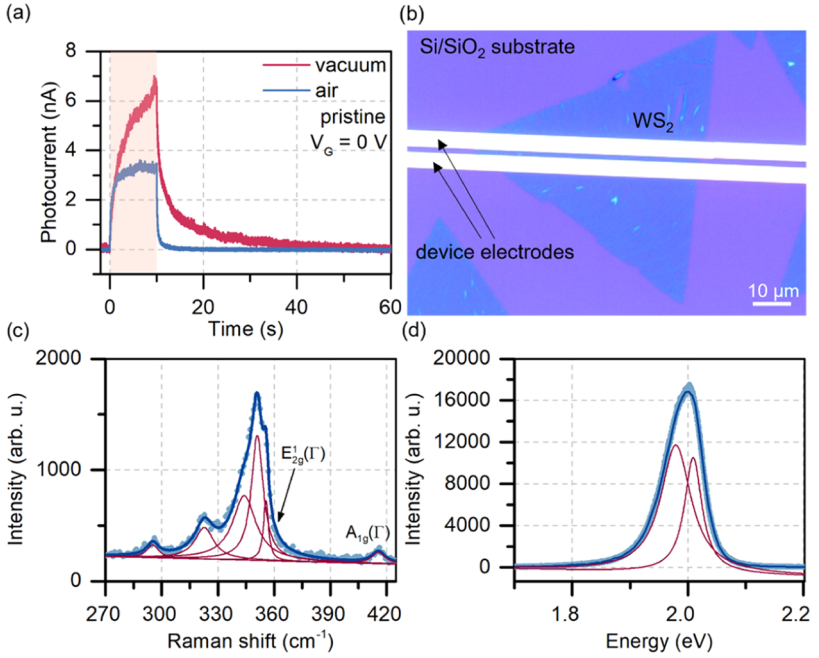

Figure 1. Initial characterization of the as-prepared WS_2 sample. (a) Time-resolved photocurrent signal of the pristine WS_2 sample in vacuum and air. The highlighted area corresponds to the time the device was illuminated. (b) Optical image showing the measured device. The channel was 2 μm long. (c, d) Raman spectrum (c) and photoluminescence spectrum (d) of the WS_2 untreated sample were measured with a 532 nm laser. The spectra show the fitted Lorentzian functions for the specific peaks (red curves).

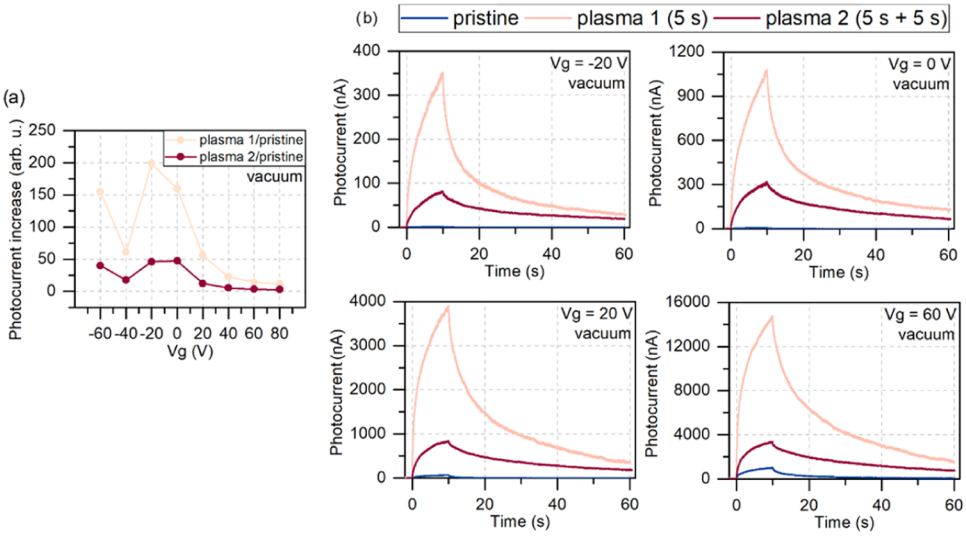

Figure 2. Comparison of the photocurrent measured in vacuum for treated and untreated samples. (a) Photocurrent increase calculated as a maximum photocurrent obtained after the same amount of time for each gate voltage and normalized by the maximum photocurrent of the pristine sample on WS_2. The results show that the devices treated with a single plasma process respond stronger to illumination, and their response is the highest for low gate voltages. (b) The photocurrent signal of the samples before (pristine—blue lines) and after plasma treatment (first plasma—beige lines, second plasma—red lines) measured in vacuum. The graphs show the gate voltage dependence of the photocurrent for −20, 0, 20, and 60 V. Large enhancement of the photocurrent was observed after the first plasma treatment. The second plasma treatment also increased the signal compared to the pristine sample, but the effect was not as pronounced as for the first treatment. Although the point at −40 V results from a random unexpected event, the trend is visible.

photocurrent in relation to measurements performed in air and vacuum for WS_2 and MoS_2.

In the light of the aforementioned reports, we argue that the photocurrent enhancement of the TMD samples is a combined result of vacancy creation and oxide formation on the sample. In this work, we show on-chip tuning of the photocurrent response of WS_2 to significantly enhance the electrical signal while elongating the duration of the PPC under UV illumination. The tuning effect is obtained by mild plasma exposure, which forms a few kinds of structures upon the sample: sulfur vacancies, nonstoichiometric transition metal oxide (TMO), and stoichiometric TMO. We show that the significant effect of photocurrent enhancement (over 150 times) stems from the optimized plasma process and the well-matched wavelength of the light used in our experiment that fits in the band-gap region of both TMDs and TMO. We also

https://doi.org/10.1021/acsami.2c06578
ACS Appl. Mater. Interfaces 2022, 14, 33984−33992

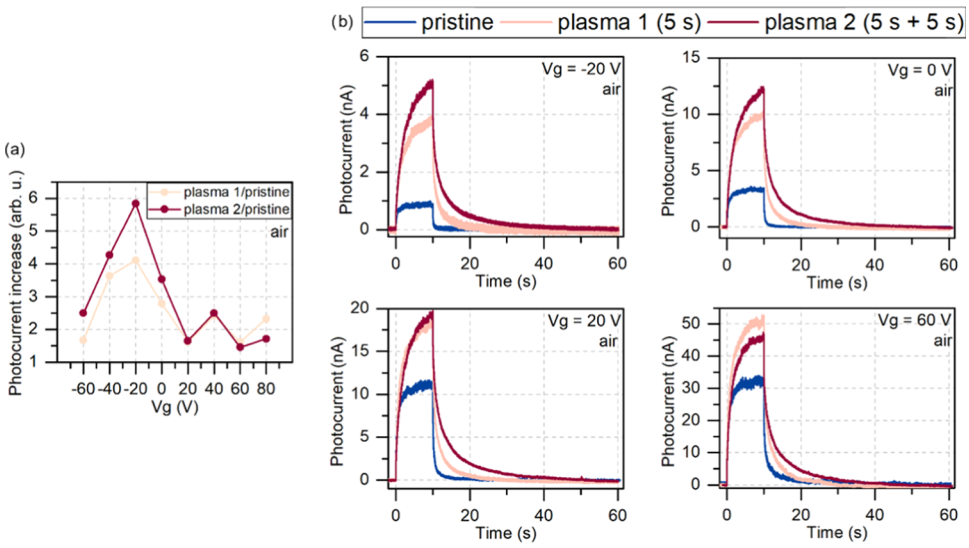

Figure 3. Comparison of the photocurrent measured in air for treated and untreated samples. (a) Photocurrent increase calculated as a maximum photocurrent obtained after the same amount of time for each gate voltage and normalized by the maximum photocurrent of the pristine sample in air. (b) The photocurrent signal of the samples before (pristine—blue lines) and after plasma treatment (first plasma—beige lines, second plasma—red lines) measured in air. The graphs show the gate voltage dependence of the photocurrent for −20, 0, 20, and 60 V. The photocurrent signal shows a stronger dependence on the applied voltage in air, where the dominating signal changes between the second and first plasma treatments. The highest photocurrent enhancement was observed for low gate voltages after two plasma processes. Still, with a high gate voltage applied, the first plasma treatment yields the best results in increasing the signal (here at 60 V).

show that both oxide formation and the created vacancies in the sample increase the charge trapping mechanism.

Contrary to previous work on plasma-enhanced photocurrent generation in TMDs,[12] we show the impact of the environment on the enhancing effect by employing photocurrent measurements in vacuum and air. Moreover, no photocurrent enhancement has ever been shown for WS_2 monolayers under plasma treatment. No such high photocurrent increase has ever been shown for the plasma-treated monolayers of TMDs as well.

The plasma treatment and electrical measurements were also conducted for the MoS_2 sample, and the results are consistent with WS_2 measurements, suggesting the versatility of the modification method. Our work contributes to learning the tuning effect for creating optoelectronic devices that can be tailored to the desired properties, enabling multitudes of future applications, especially as optoelectronic memories or artificial optical synapses.

RESULTS AND DISCUSSION

Pristine monolayer WS_2 devices were first measured electrically in vacuum and air. The time-resolved photocurrent on devices based on WS_2 in both environments was of the same order of magnitude, as shown in Figure 1. The rise and decay of the photocurrent followed the typical behavior of such devices—slower responses were observed in vacuum due to the lack of environmental adsorbates, which assist in relaxation.[18] Raman and photoluminescence spectroscopy results and the optical image of the device are shown in Figure 1. The Raman spectra show typical Raman peaks of WS_2 in resonance for a 532 nm laser. The observed feature is a combination of six peaks, including A_{1g} at ∼417 cm^{-1}, E^1_{2g} at 356 cm^{-1}, and the most intense 2LA at 350 cm^{-1}. Photoluminescence shows a highly intense peak typical for the monolayer material, fitted with two Lorentzian curves following the literature reports, showing the occurrence of neutral and negative excitons.[19,20]

Next, the samples underwent a plasma process (the details are in the Methods section). Two plasma processes were done in total on the samples. The first treatment was for 5 s (called plasma 1 in further text), and then the sample was measured in vacuum and air. Next, it was subjected to another 5 s of plasma treatment (plasma 2 in further text) and measured. Figure 2 shows the photocurrent measured on the WS_2 sample before and after the first (5 s) and second (5 s + 5 s) plasma processes in vacuum under different gate biases. The applied gate voltages ranged from −60 to 80 V with a step of 20 V for the time-resolved photocurrent measurement.

We see that the plasma process significantly changed the photoresponse of the devices. After the first plasma treatment, we obtained over 150 times enhancement of the photocurrent value compared to the pristine sample of WS_2 at zero gate bias (from 6.9 nA to 1.1 μA). It is a record value of photocurrent enhancement by plasma treatment in TMD monolayers. In vacuum, the dominating photocurrent signal comes after the first plasma process for both positive and negative gate bias. The second treatment decreased the signal to 50-fold enhancement compared to the pristine sample. We calculated the responsivity with the formula $\Re = \frac{I_{photo}}{P_{opt}}$, where I_{photo} is the measured photocurrent and P_{opt} is the optical power of light. The values at zero gate bias for the samples pristine, after plasma 1, and after plasma 2 were 0.05, 166, and 6.5 mA/W, respectively.

The exact measurements were repeated for the sample in air and are shown in Figure 3. In the air, we also see the photocurrent enhancement; however, the signal strength behaves quite differently than that in vacuum.

Surprisingly, the photocurrent enhancement in air is much less impressive (below 3 and 3.5 times at zero gate bias for the first and second treatment, respectively), but it shows a gate voltage dependence. For negative and relatively low gate voltages (up to 20 V), the second plasma treatment resulted in

https://doi.org/10.1021/acsami.2c06578
ACS Appl. Mater. Interfaces 2022, 14, 33984−33992

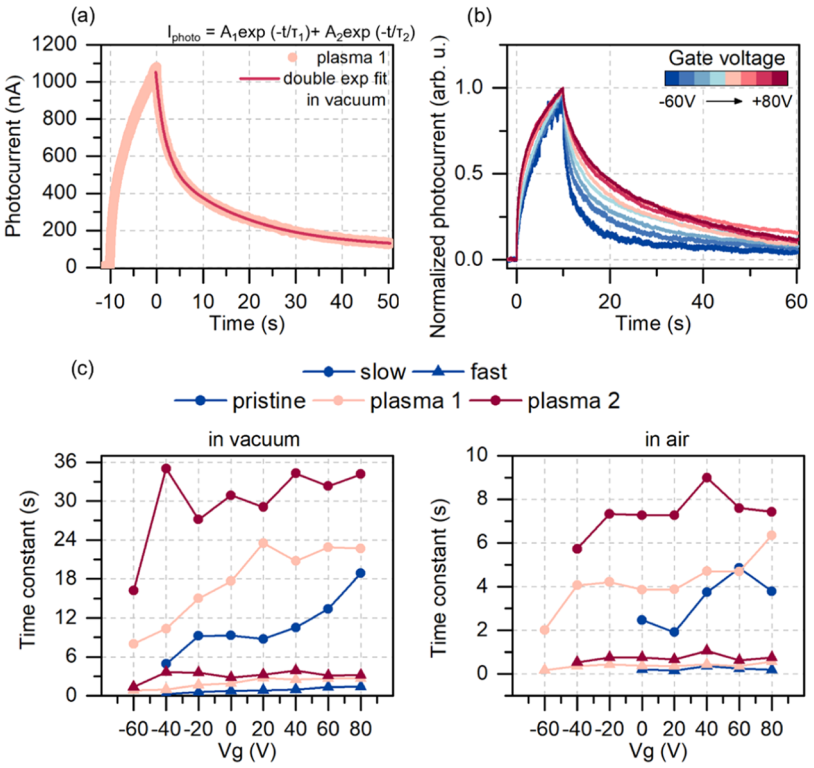

Figure 4. Relaxation time dependence on the gate voltage. (a) The result of fitting a double exponential function to the photocurrent decay signal of the plasma-treated sample. (b) Normalized photocurrent signal of the sample after the first plasma treatment in vacuum showing the effect of the applied gate voltage on the photocurrent relaxation in the sample. The lower the gate voltage applied, the faster the relaxation. This effect is attributed to the occupancy of the recombination centers in the band gap. (c) The slow and fast photoresponse time constants for each sample resulting from the double exponential fit in (a). The slow component shows a stronger dependence on the applied gate voltage. The significant noise for the untreated sample at low voltages in air resulted in the inability to perform the fit and therefore missing points in the plot.

a dominating photocurrent signal. This changes at a gate bias of 40 V when both signals are almost equal, and for higher gate voltages, the dominating one is the signal after the first plasma treatment. To the best of our knowledge, such intriguing dependence of photocurrent enhancement on the environment and gate voltage has never been explored. Similar behavior of the MoS_2 samples is shown in Figures S1 and S2. A complete comparison between photocurrents measured for WS_2 at all applied gate voltages is shown in Figure S3. The responsivity values calculated at zero gate voltage for the samples pristine, after plasma 1, and after plasma 2 were 25, 77, and 92 μA/W, respectively.

We also found that the plasma treatment influenced the relaxation times of the photocurrent. We fitted the photocurrent decay after the illumination was turned off with a double exponential function,[3,11,21] which resulted in obtaining two time constants corresponding to fast and slow contribution to the signal (see Figure 4). The fitting formula was $I_{photo} = A_1 exp\left(-\frac{t}{\tau_1}\right) + A_2 exp\left(-\frac{t}{\tau_2}\right)$, where τ_1 and τ_2 are the time constants of the fit and A_1 and A_2 are the amplitudes. After each plasma process at zero gate bias, the photocurrent decay time components almost doubled in the response time in both environments. The considerable photocurrent enhancement comes, therefore, with a cost of a slower photoresponse. Such an exchange would be beneficial for several applications such as UV-enhanced gas sensors, emerging visible light positioning systems not requiring millisecond precision, optoelectronic memories, and synapses to set the information storage time to the desired value. The response time can also be partially controlled by applying a gate voltage, as shown in Figure 4. Low gate voltage applied results in faster relaxation. The decay time increases for high gate voltage applied. Figure 4c shows the time constants obtained at each gate voltage applied. The slow component exhibits a substantial increase in value for each plasma treatment and increases with higher gate voltages. The fast component (usually attributed to the photoconductive effect) roughly doubles in its value after each plasma treatment but does not show such a strong dependence on the gate voltage. The slow component's gate dependence suggests its relation to trap states in the band gap. Pushing the Fermi level toward the valence band (applying negative gate voltage) results in more unoccupied states within the energy band gap. These states act as additional recombination centers for excited electrons. At high gate voltage with the increasing Fermi level, more and more states are occupied, and therefore, the recombination time is longer, as previously reported.[22] So, the response time of such a device can be partially controlled by the dielectric gate. The distinction between recombination centers and trap states should be considered because it is the latter that causes the increase of the response time in both components by trapping the photogenerated charge carriers. The reason for the increase of the response time, while simultaneously observing the decrease of the photocurrent after the second plasma treatment, is hypothesized that although the sample with more structural defects can trap the photogenerated electrons for a longer period, the photocurrent generation becomes less effective due to the introduction of too many defects to the crystal structure.

https://doi.org/10.1021/acsami.2c06578
ACS Appl. Mater. Interfaces 2022, 14, 33984−33992

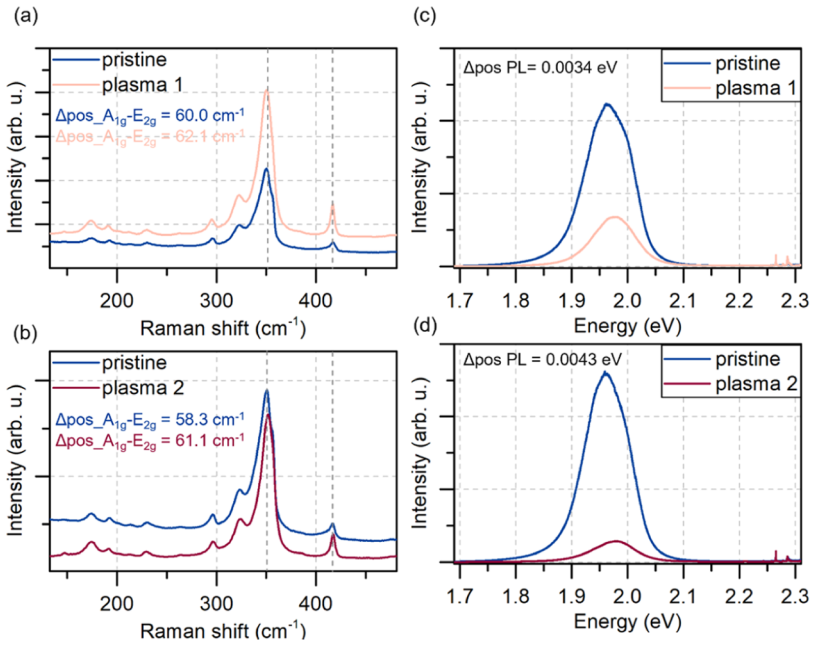

Figure 5. Raman and photoluminescence spectroscopy results. (a, b) Raman spectra of the untreated (pristine) and plasma-treated samples of WS_2 (one plasma process—a, two plasma processes—b). The treatment of the samples resulted in the asymmetric shift of the two main peaks (upshift of A_{1g}, downshift of E^1_{2g}), changing the difference in peaks' positions (Δpos $A_{1g}-E_{2g}$). (c, d) Photoluminescence spectra of WS_2 untreated and treated samples. The plasma treatment resulted in the signal quenching and the blue shift of the peaks by Δpos PL = 0.0034 eV (c) after the first plasma process and 0.0043 eV (d) after the second plasma process. The position of the peak was calculated as the mean value of the two fitted Lorentzian curves.

As a result of the plasma treatment, we also noticed an enlargement in the hysteresis of the transfer characteristics of the WS_2 FET and a shift of the threshold voltage in transfer characteristics under illumination. These changes are shown in Figure S4. The hysteresis results from carrier trapping in TMD layers, either extrinsic (adsorbates) or intrinsic (trap states).[23,24]

The observed outcome of photocurrent enhancement and decay time change could be attributed to several effects and require further discussion. The first expected effect could be an introduction of sulfur vacancies, which will be discussed in more detail in the next paragraph. The second one could be attributed to the creation of TMOs in their stoichiometric and nonstoichiometric forms. Indeed, it was already observed that the oxygen plasma treatment forms a transition metal oxide on the surface of MoS_2.[25,26] The mechanism previously attributed to the TMO photocurrent enhancement in MoS_2 was the formation of MoS_2-MoO_{3-x} junctions, which serve as carrier trapping sites. These randomly formed TMOs in their stoichiometric form have band gaps of ~3 eV depending on the fabrication method and annealing, for example, MoO_3 (3.03,[27] 3.14 eV[28]) and WO_3 (2.97,[29] 3.24 eV[30]). Nonstoichiometric WO_{3-x} oxides were shown to have lower band gaps (3.1, 2.6 eV) depending on the oxygen pressure in the growth process.[31] These energies of band gaps are just below the illumination wavelength used in our experiment, which is ~3.4 eV (365 nm). Both WO_3 and MoO_3 in their nonstoichiometric form were shown to generate photocurrent.[31,32] Thus, the formed oxide in our samples may also be responsible for electron–hole pair generation, contributing to the total photocurrent enhancement. To prove the above hypothesis and compare the versatility of the plasma treatment enhancement on TMDs, we measured the photocurrent on another sample. Here, we repeat the experiment on MoS_2 instead of the WS_2-based device under two different wavelengths (365 nm and 533 nm/2.33 eV) to see if the same plasma parameters would also induce such a high photocurrent enhancement as in the previous samples (see Figure S5). Indeed, it was confirmed that the enhancement in UV light was stronger than that in green light, despite the initially almost equal signal values, most likely due to the light energy above the band gap of MoO_3.

Now, we focus on the environmental impact on the treated samples. The environmental dependence is seen as the difference between the first and second plasma treatments in air and vacuum (Figure 3) and also shows the strong relationship of the photocurrent with environmental adsorbates, suggesting a significant influence on the structural defects with sulfur vacancies being the most common.[33] Defect sites are the optimal spots for the environmental molecules' adsorption on the surface of the sample.[14,34,35] Sulfur vacancies could be introduced in our material by the nonreactive argon plasma, which was half of the gas mixture used in the process. These defects were also shown to cause the occurrence of the additional trap states in the WS_2 band gap.[36,37] The adsorbed environmental molecules (O_2, H_2O) on the device in the dark limit its electrical performance by trapping the electrons flowing through the channel. Positive gate bias causes oxygen and water adsorption on the sample, whereas these molecules are desorbed at negative gate voltages.[38] So the performance of the TMD-based FETs in the air in the dark, despite applying high gate voltages and thus increasing the electron density in the channel, is still strongly hindered due to charge trapping in the adsorbed molecules.[38] Upon illumination, these trapped electrons can recombine with photogenerated holes, resulting in increased current by photogenerated electrons remaining unrecombined in the channel. These photogenerated electrons may be trapped by adsorbate traps and then again recombine

https://doi.org/10.1021/acsami.2c06578
ACS Appl. Mater. Interfaces 2022, 14, 33984−33992

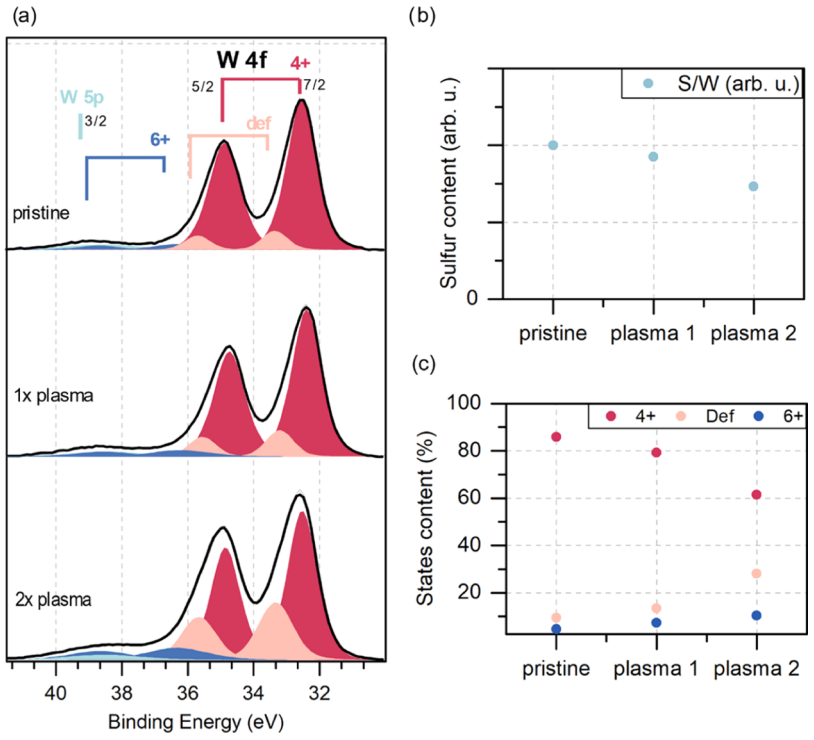

Figure 6. XPS measurements results. (a) XPS spectra with fitted peaks. (b) Relative differences in the S/W ratio of the untreated and plasma-treated samples. (c) Percentages of the individual states in the sample before and after the plasma treatment.

with photogenerated holes, which is the reason for a gradual, slow rise of the photocurrent in the time domain until these processes of adsorption and desorption reach equilibrium.[39,40]

The remarkable environment-dependent difference between the first and second plasma treatments confirms the effects of the gate-bias-induced molecules' adsorption and desorption processes in photogeneration.[38,39] In the air, under low gate voltage bias, the dominating photocurrent signal was after the second plasma treatment. Low gate voltage applied means that there are still unfilled traps in the band gap and fewer surface adsorbates on the TMD sample. Two plasma processes are likely to result in more sulfur vacancies, leading to the formation of trap states in the gap.[36] The trap states keep the photogenerated carriers for a longer time, resulting in higher photocurrent and slower time response.[22] Applying higher gate voltages results in the increase of the Fermi level and filling of trap states, which are attributed to be the main reason for the photocurrent enhancement after the second plasma treatment.[22] Therefore, the dominating signal becomes the photocurrent after the first plasma treatment.

The lower photocurrent enhancement after the second plasma treatment in vacuum is most likely caused by the effect of too many defects. The sample after the first plasma treatment has the balance of the efficient photocurrent generation of the direct band gap, more stoichiometric TMD (WS_2) with the small addition of the favorable defect states due to atomic vacancies, heterojunctions with TMO, and TMO itself under UV light. After the second plasma treatment, the sample has even more trap states and even more oxidized areas, which we can observe as the further increase of the relaxation time of the photocurrent. However, the photocurrent generation and current flow of such a sample are reduced because of large numbers of oxide intrusions, which in larger quantities are less effective in terms of photocurrent generation and sample conductivity. The balance between TMD, TMO, and trap states is disturbed, leading to the lowering of the device performance.

The photocurrent enhancement seen in our samples could be attributed to sulfur vacancies (along with the introduced trap states in the band gap), nonstoichiometric TMOs resulting in traps at the formed junction, and stoichiometric TMO formation with the optimal choice of illumination wavelength. To further verify any of the mentioned possibilities, Raman, photoluminescence, and X-ray photoelectron spectroscopy (XPS) spectra were taken on both WS_2 and MoS_2 samples before and after the first and second plasma processes. The Raman and photoluminescence average results of the statistical mapping (121 points) for the WS_2 sample are shown in Figure 5. Similar results for the MoS_2 sample are shown in Figure S6 in the Supporting Information.

In both TMDs, in Raman spectra, we observed a slight red shift of the E^1_{2g} peak and a blue shift of A_{1g} peak, increasing the difference in these two peaks' positions. Such an asymmetric change in the Raman spectrum was previously ascribed to the formation of the TMO on the sample.[12,41,42] The blue shift of the A_{1g} peak results from p-type doping (by built-in oxygen),[43] whereas the change of E^1_{2g} is described as a distortion of the crystal lattice and the change of the out-of-plane vibration of sulfur atoms.[26] The peaks' width also changes (their broadening would be expected[26]), but these changes are a bit more challenging to address for WS_2 due to the occurring resonance at 532 nm (the matter is further described in the Supporting Information, the individual points of the mapping measurement are shown in Figure S7). The plasma treatment was optimized for WS_2 by repeated measurements at different plasma process settings. For MoS_2, the treatment was stronger, and the process details are explained in the Supporting Information (see Figures S6 and S7). Still, despite the strong

https://doi.org/10.1021/acsami.2c06578
ACS Appl. Mater. Interfaces 2022, 14, 33984−33992

treatment, the enhancement mechanisms occurred in both samples. Both materials undergo structural changes, along with the expected oxidation. The average photoluminescence spectrum of WS_2 was also quenched, and the peaks blue-shifted, suggesting the random oxide formation.[12,41,42] Statistical Raman results prove that the observed effect of photocurrent enhancement could not be attributed to removing the surface contaminants only. The observed spectra change significantly with each plasma treatment, and the changes correspond to the statements of our hypothesis.

To further support the data from Raman mapping and photoluminescence analysis, XPS spectra were taken on the same samples (WS_2 is shown in Figure 6 and MoS_2 is in Figure S8). The XPS measurement of W 4f and S 2p core line spectra allows us to conclude the stoichiometry changes caused by the plasma treatment. The relative differences in the S/W ratio (Figure 6b) indicate that the plasma treatment led to a significant decrease in sulfur content (over 25% after the second plasma treatment). Additionally, the visible changes in the W 4f line shape were analyzed based on the peak fitting procedure. The W 4f region contains a few different species related to different chemical states of W ions, and each state is represented by a spin−orbit doublet line ($4f_{7/2}$ and $4f_{5/2}$). The main doublet with W $4f_{7/2}$ maxima near 32.8 eV can be identified as a 4+ oxidation state, indicating the presence of 2H WS_2.[44,45] The second doublet shifted to higher binding energy (W $4f_{7/2}$ line near 36.2 eV) can be identified as coming from a 6+ state present in WO_3.[44,46] Additionally, the spectrum's shape requires a third state to be added between the previous two. This state may be related to the presence of non-stoichiometric oxides[47] or WO_2;[48] for the purposes of further discussion, this state will be called the defect state. XPS spectra with fitted peaks are presented in Figure 6a, while the percentages of individual states for the pre- and post-plasma-treated samples are summarized in Figure 6c. The analysis of the WS_2 sample shows that in each plasma process, there are fewer sulfur S 2p bonds in the material, indicating the occurrence of sulfur vacancies and the possibility of oxide formation. A slight increase of the 6+ peak proves that the traces of WO_3 can be found on the surface. There is also an intense defect state feature growing with each plasma process that cannot be entirely attributed to any stoichiometric oxides. This indicates that the plasma treatment transformed a part of W−S bonds and led to the formation of nonstoichiometric TMO (WO_{3-x}) or possibly WO_2.

The MoS_2 XPS spectra are shown in Figure S8. The results in MoS_2 lead to similar conclusions as in WS_2 samples.

CONCLUSION

In summary, we showed an extraordinary on-chip, over 150-fold enhancement of the photocurrent signal and a gradual time response modulation in WS_2 and MoS_2 monolayer-based devices by oxygen−argon plasma treatment. The treatment changes the behavior of the samples depending on the environment. The effect can be explained by the co-occurrence of several effects: charge trapping by sulfur vacancies and TMD−TMO heterojunctions, along with effective electron−hole pair generation from the favorable illumination wavelength choice for the excitement of both TMDs and TMO. This method could be used to modulate the photogeneration for the novel applications of the TMDs in optoelectronic applications such as memories, artificial synapses, or others using the effect of persistent photoconductivity or favoring the effects of a strong photocurrent signal over the time of response.

METHODS

Device Fabrication. The devices were fabricated on the chemical vapor deposition (CVD) samples of WS_2 and MoS_2 monolayers on a 300 nm SiO_2/Si substrate (Sixcarbon Technology, Shenzhen, China). We used the electron-beam lithography technique to fabricate two-terminal FET devices with a bottom gate configuration, a 2 μm long channel, and 5 nm chromium/100 nm thick gold electrodes thermally evaporated.

Plasma Treatment and Structural Characterization. The plasma process was done using Diener Zepto plasma with an argon−oxygen gas mix in equal proportion. The plasma parameters 4 W, 15 sccm, and 5 s were chosen after a series of optimization measurements. Raman spectroscopy and photoluminescence measurements were done with a 532 nm laser (Renishaw inVia Qontor Raman spectrometer) on the samples after each plasma process. Different samples were used for electrical measurements and spectroscopic measurements.

Electrical Measurements. Electrical measurements were done using a DL-1211 Current Preamplifier and National Instruments DAQ 6366 with a sampling frequency of 1 kHz. We used Oxford MicrostatHe2 cryostat to provide a vacuum environment for the sample before the measurements for ∼16 h. The pressure was at least 5×10^{-3} mbar or lower. For measurements in air, the cryostat was vented, maintaining the cover with a glass window to avoid differences in light scattering. All photocurrent measurements were done applying 5 V source−drain bias. The illumination was provided by a 365 nm LSM diode with an LDC-1 controller (Ocean Insight) for 10 s each. The light power on the sample was 130 μW. For wavelength-dependent measurements, 365 nm and 533 nm LSM diodes were used, operating at an optical power of 30 μW.

XPS Measurements. The results were supplemented by XPS. The XPS system was equipped with a hemispherical energy analyzer Phoibos 150 (SPECS) with a 2D-CCD detector and a DAR 400 X-ray lamp (Omicron); nonmonochromatic radiation of 1253.64 eV (Mg Kα) was used. The peak fitting procedure was supported by Casa XPS software.

ASSOCIATED CONTENT

Supporting Information

The Supporting Information is available free of charge at https://pubs.acs.org/doi/10.1021/acsami.2c06578.

Photocurrent results obtained for MoS_2 samples in both environments; showcase of complete results for WS_2 samples under different gate voltages; transfer characteristics for WS_2 and MoS_2 FETs; photocurrent measurements of MoS_2 under green light illumination; Raman and photoluminescence spectra of the samples before and after plasma treatment; and XPS results of the MoS_2 sample (PDF)

AUTHOR INFORMATION

Corresponding Author

Karolina Czerniak-Łosiewicz − *Faculty of Physics, Warsaw University of Technology, 00-662 Warsaw, Poland;* orcid.org/0000-0002-6781-9374; Phone: +48 22 234 75 46; Email: karolina.czerniak@pw.edu.pl

Authors

Michał Świniarski − *Faculty of Physics, Warsaw University of Technology, 00-662 Warsaw, Poland*

Arkadiusz P. Gertych − *Faculty of Physics, Warsaw University of Technology, 00-662 Warsaw, Poland;* orcid.org/0000-0002-7740-9651

https://doi.org/10.1021/acsami.2c06578
ACS Appl. Mater. Interfaces 2022, 14, 33984−33992

Małgorzata Giza − *Faculty of Physics, Warsaw University of Technology, 00-662 Warsaw, Poland*
Zofia Maj − *Faculty of Physics, Warsaw University of Technology, 00-662 Warsaw, Poland*
Maciej Rogala − *Faculty of Physics and Applied Informatics, University of Lodz, 90-236 Lodz, Poland;* orcid.org/0000-0002-7898-5087
Paweł J. Kowalczyk − *Faculty of Physics and Applied Informatics, University of Lodz, 90-236 Lodz, Poland;* orcid.org/0000-0001-6310-4366
Mariusz Zdrojek − *Faculty of Physics, Warsaw University of Technology, 00-662 Warsaw, Poland*

Complete contact information is available at: https://pubs.acs.org/10.1021/acsami.2c06578

Author Contributions

K.C.-Ł. conceived the project and designed the experiment. K.C.-Ł., M.Ś., and M.G. fabricated the devices and performed electrical measurements. A.P.G., Z.M., and K.C.-Ł. performed Raman and photoluminescence spectroscopic measurements. M.R. and P.J.K. performed XPS measurements and discussed the findings. K.C.-Ł., M.S., A.P.G., M.G., and M.Z. analyzed and discussed the data. M.Z. supervised the project. K.C.-Ł. wrote the manuscript and all co-authors took part in the writing process.

Notes

The authors declare no competing financial interest.

■ ACKNOWLEDGMENTS

This research was supported by the PRELUDIUM project (UMO-2020/37/N/ST5/00747), MINIATURA project (MINIATURA-DEC-2020/04/X/ST5/01453), and SONATA BIS project (2020/38/E/ST3/00293) by the National Science Centre, Poland. Part of this research was funded by POB Technologie Materialowe of Warsaw University of Technology within the Excellence Initiative: Research University (IDUB) programme. The authors acknowledge the support of the EU Graphene Flagship funding (Grant Graphene Core3 No. 881603).

■ ABBREVIATIONS

TMDs, transition metal dichalcogenides
WS_2, tungsten disulfide
MoS_2, molybdenum disulfide
PPC, persistent photoconductivity
FETs, field-effect transistors
TMO, transition metal oxide
WO_3, tungsten oxide
MoO_3, molybdenum oxide
O_2, oxygen
H_2O, water
XPS, X-ray photoelectron spectroscopy
CVD, chemical vapor deposition

■ REFERENCES

(1) Wang, Q. H.; Kalantar-Zadeh, K.; Kis, A.; Coleman, J. N.; Strano, M. S. Electronics and Optoelectronics of Two-Dimensional Transition Metal Dichalcogenides. *Nat. Nanotechnol.* **2012**, *7*, 699−712.
(2) Lim, Y. R.; Song, W.; Han, J. K.; Lee, Y. B.; Kim, S. J.; Myung, S.; Lee, S. S.; An, K. S.; Choi, C. J.; Lim, J. Wafer-Scale, Homogeneous MoS2Layers on Plastic Substrates for Flexible Visible-Light Photodetectors. *Adv. Mater.* **2016**, *28*, 5025−5030.
(3) Di Bartolomeo, A.; Genovese, L.; Foller, T.; Giubileo, F.; Luongo, G.; Croin, L.; Liang, S. J.; Ang, L. K.; Schleberger, M. Electrical Transport and Persistent Photoconductivity in Monolayer MoS2 Phototransistors. *Nanotechnology* **2017**, *28*, No. 214002.
(4) Lopez-Sanchez, O.; Lembke, D.; Kayci, M.; Radenovic, A.; Kis, A. Ultrasensitive Photodetectors Based on Monolayer MoS 2. *Nat. Nanotechnol.* **2013**, *8*, 497−501.
(5) Furchi, M. M.; Polyushkin, D. K.; Pospischil, A.; Mueller, T. Mechanisms of Photoconductivity in Atomically Thin MoS2. *Nano Lett.* **2014**, *14*, 6165−6170.
(6) Luo, Z. D.; Xia, X.; Yang, M. M.; Wilson, N. R.; Gruverman, A.; Alexe, M. Artificial Optoelectronic Synapses Based on Ferroelectric Field-Effect Enabled 2D Transition Metal Dichalcogenide Memristive Transistors. *ACS Nano* **2020**, *14*, 746−754.
(7) Zhou, F.; Zhou, Z.; Chen, J.; Choy, T. H.; Wang, J.; Zhang, N.; Lin, Z.; Yu, S.; Kang, J.; Wong, H. S. P.; Chai, Y. Optoelectronic Resistive Random Access Memory for Neuromorphic Vision Sensors. *Nat. Nanotechnol.* **2019**, *14*, 776−782.
(8) Islam, M. M.; Dev, D.; Krishnaprasad, A.; Tetard, L.; Roy, T. Optoelectronic Synapse Using Monolayer MoS2 Field Effect Transistors. *Sci. Rep.* **2020**, *10*, No. 21870.
(9) Xiang, D.; Liu, T.; Xu, J.; Tan, J. Y.; Hu, Z.; Lei, B.; Zheng, Y.; Wu, J.; Neto, A. H. C.; Liu, L.; Chen, W. Two-Dimensional Multibit Optoelectronic Memory with Broadband Spectrum Distinction. *Nat. Commun.* **2018**, *9*, No. 2966.
(10) Lei, S.; Wen, F.; Li, B.; Wang, Q.; Huang, Y.; Gong, Y.; He, Y.; Dong, P.; Bellah, J.; George, A.; Ge, L.; Lou, J.; Halas, N. J.; Vajtai, R.; Ajayan, P. M. Optoelectronic Memory Using Two-Dimensional Materials. *Nano Lett.* **2015**, *15*, 259−265.
(11) George, A.; Fistul, M. V.; Gruenewald, M.; Kaiser, D.; Lehnert, T.; Mupparapu, R.; Neumann, C.; Hübner, U.; Schaal, M.; Masurkar, N.; Arava, L. M. R.; Staude, I.; Kaiser, U.; Fritz, T.; Turchanin, A. Giant Persistent Photoconductivity in Monolayer MoS2 Field-Effect Transistors. *npj 2D Mater. Appl.* **2021**, *5*, No. 15.
(12) Jadwiszczak, J.; Li, G.; Cullen, C. P.; Wang, J. J.; Maguire, P.; Duesberg, G. S.; Lunney, J. G.; Zhang, H. Photoresponsivity Enhancement in Monolayer MoS2 by Rapid O2:Ar Plasma Treatment. *Appl. Phys. Lett.* **2019**, *114*, No. 091103.
(13) do Nascimento Barbosa, A.; Mendoza, C. A. D.; Figueroa, N. J. S.; Terrones, M.; Freire Júnior, F. L. Luminescence Enhancement and Raman Characterization of Defects in WS2 Monolayers Treated with Low-Power N2 Plasma. *Appl. Surf. Sci.* **2021**, *535*, No. 147685.
(14) Jiang, J.; Zhang, Q.; Wang, A.; Zhang, Y.; Meng, F.; Zhang, C.; Feng, X.; Feng, Y.; Gu, L.; Liu, H.; Han, L. A Facile and Effective Method for Patching Sulfur Vacancies of WS2 via Nitrogen Plasma Treatment. *Small* **2019**, *15*, No. 1901791.
(15) Hou, J.; Ke, C.; Chen, J.; Sun, B.; Xia, Y.; Li, X.; Chen, T.; Wu, Y.; Wu, Z.; Kang, J. Reduced Turn-on Voltage and Boosted Mobility in Monolayer Ws2 Transistors by Mild Ar+ Plasma Treatment. *ACS Appl. Mater. Interfaces* **2020**, *12*, 19635−19642.
(16) Di Bartolomeo, A.; Urban, F.; Faella, E.; Grillo, A.; Pelella, A.; Giubileo, F.; Askari, M. B.; McEvoy, N.; Gity, F.; Hurley, P. K. PtSe2 Phototransistors with Negative Photoconductivity. *J. Phys.: Conf. Ser.* **2021**, *1866*, No. 012001.
(17) Grillo, A.; Faella, E.; Pelella, A.; Giubileo, F.; Ansari, L.; Gity, F.; Hurley, P. K.; McEvoy, N.; DiBartolomeo, A. Coexistence of Negative and Positive Photoconductivity in Few-Layer PtSe2 Field-Effect Transistors. *Adv. Funct. Mater.* **2021**, *31*, No. 2105722.
(18) Zhang, W.; Huang, J. K.; Chen, C. H.; Chang, Y. H.; Cheng, Y. J.; Li, L. J. High-Gain Phototransistors Based on a CVD MoS2 Monolayer. *Adv. Mater.* **2013**, *25*, 3456−3461.
(19) Cui, Q.; Luo, Z.; Cui, Q.; Zhu, W.; Shou, H.; Wu, C.; Liu, Z.; Lin, Y.; Zhang, P.; Wei, S.; Yang, H.; Chen, S.; Pan, A.; Song, L. Robust and High Photoluminescence in WS2 Monolayer through In Situ Defect Engineering. *Adv. Funct. Mater.* **2021**, *31*, No. 2105339.
(20) Chow, P. K.; Jacobs-Gedrim, R. B.; Gao, J.; Lu, T. M.; Yu, B.; Terrones, H.; Koratkar, N. Defect-Induced Photoluminescence in Monolayer Semiconducting Transition Metal Dichalcogenides. *ACS Nano* **2015**, *9*, 1520−1527.

(21) Di Bartolomeo, A.; Grillo, A.; Urban, F.; Iemmo, L.; Giubileo, F.; Luongo, G.; Amato, G.; Croin, L.; Sun, L.; Liang, S. J.; Ang, L. K. Asymmetric Schottky Contacts in Bilayer MoS2 Field Effect Transistors. *Adv. Funct. Mater.* **2018**, *28*, No. 1800657.
(22) Kufer, D.; Konstantatos, G. Highly Sensitive, Encapsulated MoS2 Photodetector with Gate Controllable Gain and Speed. *Nano Lett.* **2015**, *15*, 7307−7313.
(23) Late, D. J.; Liu, B.; Matte, H. S. S. R.; Dravid, V. P.; Rao, C. N. R. Hysteresis in Single-Layer MoS 2 Field Effect Transistors. *ACS Nano* **2012**, *6*, 5635−5641.
(24) Datye, I. M.; Gabourie, A. J.; English, C. D.; Smithe, K. K. H.; McClellan, C. J.; Wang, N. C.; Pop, E. Reduction of Hysteresis in MoS2 Transistors Using Pulsed Voltage Measurements. *2D Mater.* **2019**, *6*, No. 011004.
(25) Ko, T. Y.; Jeong, A.; Kim, W.; Lee, J.; Kim, Y.; Lee, J. E. On-stack two-dimensional conversion of MoS2 into MoO3. *2D Mater.* **2017**, *4*, No. 014003.
(26) Choudhary, N.; Islam, M. R.; Kang, N.; Tetard, L.; Jung, Y.; Khondaker, S. I. Two-Dimensional Lateral Heterojunction through Bandgap Engineering of MoS2 via Oxygen Plasma. *J. Phys.: Condens. Matter* **2016**, *28*, No. 364002.
(27) Hussain, Z. Optical and Electrochromic Properties of Annealed Lithium-Molybdenum-Bronze Thin Films. *J. Electron. Mater.* **2002**, *31*, 615−630.
(28) Lee, Y. J.; Nichols, W. T.; Kim, D. G.; Kim, Y. D. Chemical Vapour Transport Synthesis and Optical Characterization of MoO3 Thin Films. *J. Phys. D: Appl. Phys.* **2009**, *42*, No. 115419.
(29) Subrahmanyam, A.; Karuppasamy, A. Optical and Electrochromic Properties of Oxygen Sputtered Tungsten Oxide (WO3) Thin Films. *Sol. Energy Mater. Sol. Cells* **2007**, *91*, 266−274.
(30) Lethy, K. J.; Beena, D.; Vinod Kumar, R.; Mahadevan Pillai, V. P.; Ganesan, V.; Sathe, V. Structural, Optical and Morphological Studies on Laser Ablated Nanostructured WO 3 Thin Films. *Appl. Surf. Sci.* **2008**, *254*, 2369−2376.
(31) Khan, A.; Al-Muhaish, N.; Mohamedkhair, A. K.; Khan, M. Y.; Qamar, M.; Yamani, Z. H.; Drmosh, Q. A. Oxygen-Deficient Non-Crystalline Tungsten Oxide Thin Films for Solar-Driven Water Oxidation. *J. Non-Cryst. Solids* **2022**, *580*, No. 121409.
(32) Arash, A.; Ahmed, T.; Govind Rajan, A.; Walia, S.; Rahman, F.; Mazumder, A.; Ramanathan, R.; Sriram, S.; Bhaskaran, M.; Mayes, E.; Strano, M. S.; Balendhran, S. Large-Area Synthesis of 2D MoO3-x for Enhanced Optoelectronic Applications. *2D Mater.* **2019**, *6*, No. 035031.
(33) Xu, Q.; Sun, Y.; Yang, P.; Dan, Y. Density of Defect States Retrieved from the Hysteretic Gate Transfer Characteristics of Monolayer MoS 2 Field Effect Transistors. *AIP Adv.* **2019**, *9*, No. 015230.
(34) Miller, B.; Parzinger, E.; Vernickel, A.; Holleitner, A. W.; Wurstbauer, U. Photogating of Mono- and Few-Layer MoS2. *Appl. Phys. Lett.* **2015**, *106*, No. 122103.
(35) Qiu, H.; Pan, L.; Yao, Z.; Li, J.; Shi, Y.; Wang, X. Electrical Characterization of Back-Gated Bi-Layer MoS 2 Field-Effect Transistors and the Effect of Ambient on Their Performances. *Appl. Phys. Lett.* **2012**, *100*, No. 123104.
(36) Wang, Y.-H.; Ho, H.-M.; Ho, X.-L.; Lu, L.-S.; Hsieh, S.-H.; Huang, S.-D.; Chiu, H.-C.; Chen, C.-H.; Chang, W.-H.; White, J. D.; Tang, Y.-H.; Woon, W.-Y. Photoluminescence Enhancement in WS2 Nanosheets Passivated with Oxygen Ions: Implications for Selective Area Doping. *ACS Appl. Nano Mater.* **2021**, *4*, 11693−11699.
(37) KC, S.; Longo, R. C.; Addou, R.; Wallace, R. M.; Cho, K. Impact of Intrinsic Atomic Defects on the Electronic Structure of MoS 2 Monolayers. *Nanotechnology* **2014**, *25*, No. 375703.
(38) Cho, K.; Park, W.; Park, J.; Jeong, H.; Jang, J.; Kim, T. Electric Stress-Induced Threshold Voltage Instability of Multilayer MoS2 Field Effect Transistors. *ACS Nano* **2013**, *9*, 7751−7758.
(39) Pak, J.; Min, M.; Cho, K.; Lien, D. H.; Ahn, G. H.; Jang, J.; Yoo, D.; Chung, S.; Javey, A.; Lee, T. Improved Photoswitching Response Times of MoS2 Field-Effect Transistors by Stacking p -Type Copper Phthalocyanine Layer. *Appl. Phys. Lett.* **2016**, *109*, No. 183502.
(40) Czerniak-Łosiewicz, K.; Gertych, A. P.; Świniarski, M.; Judek, J.; Zdrojek, M. Time Dependence of Photocurrent in Chemical Vapor Deposition MoS2 Monolayer - Intrinsic Properties and Environmental Effects. *J. Phys. Chem. C* **2020**, *124*, 18741−18746.
(41) Wei, X.; Yu, Z.; Hu, F.; Cheng, Y.; Yu, L.; Wang, X.; Xiao, M.; Wang, J.; Wang, X.; Shi, Y. Mo-O Bond Doping and Related-Defect Assisted Enhancement of Photoluminescence in Monolayer MoS2. *AIP Adv.* **2014**, *4*, No. 123004.
(42) Kang, N.; Paudel, H. P.; Leuenberger, M. N.; Tetard, L.; Khondaker, S. I. Photoluminescence Quenching in Single-Layer MoS2 via Oxygen Plasma Treatment. *J. Phys. Chem. C* **2014**, *118*, 21258−21263.
(43) Nan, H.; Wu, Z.; Jiang, J.; Zafar, A.; You, Y.; Ni, Z. Improving the Electrical Performance of MoS2 by Mild Oxygen Plasma Treatment. *J. Phys. D: Appl. Phys.* **2017**, *50*, No. 154001.
(44) Liu, W.; Benson, J.; Dawson, C.; Strudwick, A.; Raju, A. P. A.; Han, Y.; Li, M.; Papakonstantinou, P. The Effects of Exfoliation, Organic Solvents and Anodic Activation on the Catalytic Hydrogen Evolution Reaction of Tungsten Disulfide. *Nanoscale* **2017**, *9*, 13515−13526.
(45) Yang, W.; Wang, J.; Si, C.; Peng, Z.; Frenzel, J.; Eggeler, G.; Zhang, Z. [001] Preferentially-Oriented 2D Tungsten Disulfide Nanosheets as Anode Materials for Superior Lithium Storage. *J. Mater. Chem. A* **2015**, *3*, 17811−17819.
(46) Gao, J.; Li, B.; Tan, J.; Chow, P.; Lu, T. M.; Koratkar, N. Aging of Transition Metal Dichalcogenide Monolayers. *ACS Nano* **2016**, *10*, 2628−2635.
(47) McCreary, K. M.; Hanbicki, A. T.; Jernigan, G. G.; Culbertson, J. C.; Jonker, B. T. Synthesis of Large-Area WS 2 Monolayers with Exceptional Photoluminescence. *Sci. Rep.* **2016**, *6*, No. 19159.
(48) Huang, G.; Liu, H.; Wang, S.; Yang, X.; Liu, B.; Chen, H.; Xu, M. Hierarchical Architecture of WS2 Nanosheets on Graphene Frameworks with Enhanced Electrochemical Properties for Lithium Storage and Hydrogen Evolution. *J. Mater. Chem. A* **2015**, *3*, 24128−24138.

https://doi.org/10.1021/acsami.2c06578
ACS Appl. Mater. Interfaces 2022, 14, 33984−33992